Pattern formation in singly resonant second-harmonic generation with competing parametric oscillation

P. Lodahl and M. Saffman
Optics and Fluid Dynamics Department, Risø National Laboratory, Postbox 49, DK-4000 Roskilde, Denmark
(Received 30 October 1998; revised manuscript received 14 February 1999)

We theoretically investigate the generation of spatial patterns in intracavity second-harmonic generation. We consider a cavity with planar mirrors that is resonant at the fundamental frequency, but not at the second-harmonic frequency. A mean-field model is derived that describes the resonant fundamental field, and its coupling to a pair of nondegenerate parametric fields. The parametric fields are driven by the nonresonant second-harmonic field. Analysis indicates the existence of transverse instability of the pump field alone, as well as the possibility of simultaneous instability of the pump and the parametric fields. A range of spatial structures including periodic planforms as well as spatially localized states are found numerically. The simplicity of the singly resonant cavity makes it well suited for experimental studies. Estimates of experimental parameters necessary for observation of spatial structures are given. [S1050-2947(99)02810-3]

PACS number(s): 42.65.Sf, 42.65.Ky, 42.65.Tg

I. INTRODUCTION

Optical pattern formation has been studied intensively in the last few years [1]. Although the field started with studies of instabilities in cubicly nonlinear media, much recent attention has been directed at interactions governed by a quadratic, $\chi^{(2)}$ nonlinearity. Spatial patterns are generated under the combined action of diffraction and nonlinearity in the presence of spatial feedback. One way of introducing feedback is to allow two interacting beams to counterpropagate. Although backwards parametric interactions in quadratically nonlinear media were proposed in the 1960s [2] there is not sufficient birefringence in available materials to phase match a fundamental wave at frequency ω_1 to a counterpropagating second harmonic at frequency $\omega_2 = 2\omega_1$. Studies of pattern formation in quadratic media have, therefore, concentrated on intracavity geometries, where feedback is provided by the cavity mirrors [3–8]. An exception is the possibility of quasi-phase-matching counterpropagating beams using a periodically poled crystal, for which the corresponding transverse instabilities were studied recently [9].

The existence of spatial patterns in a $\chi^{(2)}$ mediated interaction was predicted first for the degenerate doubly resonant optical parametric oscillator (OPO) by Oppo *et al.* [3]. One mechanism for pattern formation was found to be off-axis emission of down-converted light leading to a lowering of the threshold for parametric generation when the cavity is tuned away from resonance. This mechanism comes into play when the cavity length is slightly longer than that for which the signal field is resonant. We will refer to this as positive detuning of the cavity. Stationary roll solutions are preferred in favor of phase-traveling waves due to interference between the degenerate pairs. Numerical simulations of the degenerate OPO have also revealed hexagonal patterns [3,10]. In addition, a singly resonant degenerate OPO where only the signal field is resonated has been investigated [5] and the relevance of the phase mismatch as a tuning parameter was identified. In the triply resonant nondegenerate OPO the degeneracy of the parametric pairs is broken and, consequently, traveling waves are always stable with respect to standing waves as demonstrated by Longhi on the basis of a nonlinear analysis [6]. Furthermore, a square pattern can also be stable near threshold [7]. When the cavity detuning is negative there is no lowering of the threshold for parametric generation. Nonetheless, spatial structures can be generated, and for negative detuning spatially localized states are generic [11,12].

The formation of spatial structures in doubly resonant intracavity second-harmonic generation (SHG) was studied in [8,13]. Linear stability analysis reveals the presence of four different types of instabilities leading to bistability and self-pulsing of the homogeneous solutions [14], and to both stationary and oscillating transverse instabilities. SHG is qualitatively different from the OPO since there is no threshold for frequency conversion, and some amount of both frequencies are always present, irrespective of pump power and strength of the nonlinearity. Numerical investigations of doubly-resonant SHG have demonstrated the appearance of both oscillatory and stationary patterns, including rolls, hexagons [8], and solitary structures [13]. Transverse instabilities have also been studied for type-II phase-matched SHG [15,16].

One motivation for studying spatial instabilities in $\chi^{(2)}$ media is that they are well suited for producing nonclassical states of light. Strong nonclassical temporal correlations have been generated using both the OPO [17] and SHG [18]. Since these devices can also be used for creating spatial structures there is a clear prospect of obtaining patterns with nonclassical spatial correlations, as has been emphasized by Lugiato and co-workers [19].

From an experimental point of view it is important to look for simple configurations, and this makes singly resonant SHG interesting. In this configuration the fundamental field is resonated in a cavity, while the second harmonic escapes freely. Both bistability [20], as well as nonclassical light [21,22], have already been demonstrated experimentally. In the present paper we study transverse instabilities and pattern formation in the singly resonant configuration.

A problem with the standard description of the OPO is

that a model with only one pair of down-converted frequencies may not be sufficiently general. Above oscillation threshold several down-converted pairs may experience gain, and the mutual competition between different longitudinal modes complicates the dynamical evolution [23]. Use of a single-mode pump field in SHG can be used to ensure single-mode behavior of the cavity. However, another complication may arise since the generated second harmonic field can act as a source for a nondegenerate competing parametric process. This process is important since it can suppress dynamics that would otherwise be observed. For example, the self-pulsing instability found in doubly resonant SHG in the absence of cavity detuning has been shown to be suppressed by competing parametric down conversion [24]. By introducing cavity detuning the situation becomes more complicated and the importance of the competing process depends on the detailed values of the relevant parameters [25].

Even in singly resonant SHG the competing parametric process can be above threshold and cannot, in general, be ignored. Generation of competing parametric pairs has been observed experimentally in a monolithic cavity by Schiller and co-workers both for doubly resonant [26] and singly resonant [27] SHG. Furthermore, the process has been described theoretically for the prospect of generating nonclassical light, also both in the doubly resonant [28] and the singly resonant [29] cases. In this paper we demonstrate that the parametric process can also influence significantly the pattern formation dynamics.

The paper is structured as follows. Mean-field equations describing the interaction of the pump at the fundamental frequency, and the down-converted parametric beams are derived in Sec. II A. In Sec. II B we calculate thresholds for transverse instabilities assuming the parametric beams are below threshold, and do not participate in the dynamics. The threshold for excitation of the parametric process is found in Sec. II C. Parameter regions are identified where either the transverse instability or the parametric process have the lowest threshold. The above-threshold nonlinear behavior is studied numerically in Sec. III. In Sec. III A we concentrate on parameters for which the parametric process is not excited, yet transverse instabilities exist. The numerics reveal a rich variety of spatial structures including periodic patterns and localized states. The nonlinear behavior when the parametric beams are also present is studied numerically in Sec. III B. Estimates of the experimental parameters necessary for observation of spatial structures given presently available nonlinear materials are made in Sec. IV. We conclude in Sec. V.

II. STABILITY ANALYSIS

A. Mean-field model

The propagation equations describing the second-harmonic generation and the competing parametric process can in the paraxial limit be written in the form

$$\frac{\partial \mathcal{E}_1}{\partial z} - i a_1 \nabla_\perp^2 \mathcal{E}_1 = i\kappa_1 e^{-i\Delta k z} \mathcal{E}_1^* \mathcal{E}_2, \tag{1a}$$

$$\frac{\partial \mathcal{E}_2}{\partial z} - i a_2 \nabla_\perp^2 \mathcal{E}_2 = i\kappa_2 e^{i\Delta k z} \mathcal{E}_1^2 + 2i\kappa_\pm e^{i\Delta\tilde{k} z} \mathcal{E}_+ \mathcal{E}_-, \tag{1b}$$

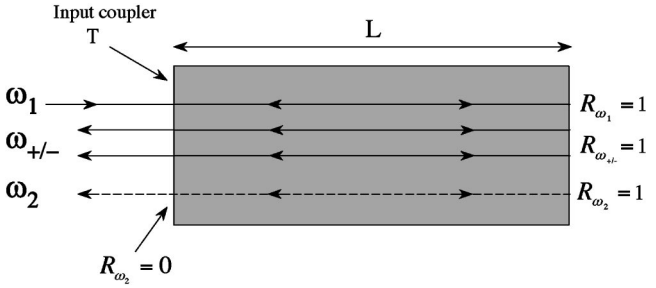

FIG. 1. The singly resonant SHG configuration in a monolithic cavity. The fundamental field ω_1 is resonated while the second harmonic ω_2 escapes after one round-trip in the cavity. Also shown are the nondegenerate resonant parametric pairs $\omega_\pm$.

$$\frac{\partial \mathcal{E}_+}{\partial z} - i a_+ \nabla_\perp^2 \mathcal{E}_+ = i\kappa_+ e^{-i\Delta\tilde{k} z} \mathcal{E}_-^* \mathcal{E}_2, \tag{1c}$$

$$\frac{\partial \mathcal{E}_-}{\partial z} - i a_- \nabla_\perp^2 \mathcal{E}_- = i\kappa_- e^{-i\Delta\tilde{k} z} \mathcal{E}_+^* \mathcal{E}_2, \tag{1d}$$

where $\mathcal{E}_1$, $\mathcal{E}_2$, and $\mathcal{E}_\pm$ denote the complex amplitudes of the fundamental, second harmonic, and down-converted fields, respectively. The real physical fields propagating along the z coordinate with wave number k_j and frequency ω_j are given by $E_j(\mathbf{r},z) = \frac{1}{2}\mathcal{E}_j(\mathbf{r}) e^{i(k_j z - \omega_j t)} + \text{c.c.}$, where $\mathbf{r} = (x,y)$ denotes the transverse coordinates, and $j = 1,2,+,-$. The phase-mismatch parameters for the SHG and the parametric process are $\Delta k = 2k_1 - k_2$ and $\Delta\tilde{k} = k_+ + k_- - k_2$, respectively. Diffraction is accounted for by the terms containing the transverse Laplacian $\nabla_\perp^2 = \partial^2/\partial x^2 + \partial^2/\partial y^2$ with coefficients $a_j = 1/(2k_j)$. In the configuration described below the parametric fields $\mathcal{E}_\pm$ are nearly degenerate with the fundamental frequency $|\omega_1 - \omega_\pm| \ll \omega_1$. Phase-matching requirements for the second-harmonic and parametric processes lead to the approximation $n \equiv n_1 \simeq n_2 \simeq n_\pm$. Under these conditions we have $a_1 \simeq 2a_2 \simeq a_\pm$ and can thus write Eqs. (1) with a single nonlinearity parameter $\kappa \equiv \kappa_1 = \kappa_2 = \kappa_\pm$.

The fundamental field is resonated in the cavity while the second harmonic is coupled out after one round-trip, as shown in Fig. 1. In the following a standing-wave monolithic cavity is considered, but the description can be extended easily to other configurations. The phase shift between the fundamental and the second harmonic at the reflecting mirror is assumed to be zero so that the cavity effectively works as a ring resonator of length $2L$, where L is the crystal length. Furthermore, a cavity with plane mirrors is considered; consequently, the homogeneous ground-state solutions are plane waves. The parametric photons will be resonant in the cavity if they are emitted at frequencies $\omega_\pm = \omega_1 \pm m\pi c/(nL)$ corresponding to a multiple of the cavity free-spectral range, where m is an integer and c is the speed of light in vacuum. The threshold for the generation of the parametric pairs will be minimized when they are emitted at frequencies close to that of the fundamental due to phase matching restrictions. Therefore, a reasonable assumption will be equal intracavity losses for the fundamental and parametric fields.

Scaled equations for the four amplitudes can be derived iteratively. Propagating the fundamental field in Eq. (1a) a length $2L$ in the crystal gives

$$\Delta\mathcal{E}_1^{\mathrm{prop}}=\mathcal{E}_1(z=2L)-\mathcal{E}_1(z=0)$$
$$=\int_0^{2L}(ia_1\nabla_\perp^2\mathcal{E}_1+i\kappa e^{-i\Delta kz}\mathcal{E}_1^*\mathcal{E}_2)dz$$
$$\simeq 2ia_1L\nabla_\perp^2\mathcal{E}_1+i\kappa\mathcal{E}_1^*\int_0^{2L}e^{-i\Delta kz}\mathcal{E}_2(z)dz. \quad (2)$$

The final equality assumes a mean-field description wherein the fundamental field $\mathcal{E}_1$ is independent of the longitudinal coordinate z. It follows from this assumption that the nonlinear and diffraction terms are only included to lowest order in a perturbative solution. The validity of this approximation is borne out both by comparison with a numerical integration of Eqs. (1) with cavity boundary conditions (see Sec. III A below) as well as consideration of physically relevant parameters. As is shown in Sec. IV the cavity field experiences small diffraction and nonlinear conversion in a single round trip under experimentally relevant conditions.

The axial dependence of the second-harmonic field, using $\mathcal{E}_2(0)=0$ and the mean-field approximation for $\mathcal{E}_1$ and $\mathcal{E}_+,\mathcal{E}_-$, is given by

$$\mathcal{E}_2(z)=\kappa\frac{e^{i\Delta kz}-1}{\Delta k}\mathcal{E}_1^2+2\kappa\frac{e^{i\Delta\tilde{k}z}-1}{\Delta\tilde{k}}\mathcal{E}_+\mathcal{E}_-. \quad (3)$$

For the moment the diffraction term in Eq. (1b) that acts on the nonresonant second-harmonic field has been neglected. The consistency of this approximation is discussed below [see Eq. (19)].

The round-trip time for propagation through the cavity is given by $\tau=2Ln/c$. The change in the intracavity field due to linear losses and phase shifts, as well as the externally supplied pump, during one cavity round-trip time is

$$\Delta\mathcal{E}_1^{\mathrm{cav}}=\tau(-\gamma_1+i\delta_1)\mathcal{E}_1+\eta\mathcal{E}_{\mathrm{in}}, \quad (4)$$

where γ_1 and $\delta_1=\omega_1-\omega_{1,c}$ ($\omega_{1,c}$ is the cavity resonance frequency closest to ω_1) are the cavity loss rate and detuning specified below and $\eta=\sqrt{T}$ determines the input coupling of the pump field to the cavity, with T the intensity transmission coefficient of the input coupler.

A mean-field equation is then obtained by combining the changes to the fundamental field from propagation and cavity effects [30]

$$\frac{\partial\mathcal{E}_1}{\partial t}\approx\frac{\Delta\mathcal{E}_1^{\mathrm{prop}}+\Delta\mathcal{E}_1^{\mathrm{cav}}}{\tau}=(-\gamma_1+i\delta_1)\mathcal{E}_1$$
$$+\frac{i\kappa\mathcal{E}_1^*}{\tau}\int_0^{2L}e^{-i\Delta kz}\mathcal{E}_2(z)dz+\frac{2ia_1L}{\tau}\nabla_\perp^2\mathcal{E}_1+\frac{\eta}{\tau}\mathcal{E}_{\mathrm{in}}, \quad (5)$$

Substituting Eq. (3) into Eq. (5) as well as the analogous equations for the parametric fields, and introducing appropriate scalings leads to the dimensionless mean-field equations,

$$\frac{\partial A_1}{\partial t}=(-1+i\Delta_1)A_1+f(\xi)|A_1|^2A_1+2h(\xi,\tilde{\xi})A_+A_-A_1^*$$
$$+i\nabla_\perp^2A_1+E, \quad (6a)$$

$$\frac{\partial A_+}{\partial t}=(-1+i\Delta_+)A_++h(\tilde{\xi},\xi)A_1^2A_-^*+2f(\tilde{\xi})|A_-|^2A_+$$
$$+i\nabla_\perp^2A_+, \quad (6b)$$

$$\frac{\partial A_-}{\partial t}=(-1+i\Delta_-)A_-+h(\tilde{\xi},\xi)A_1^2A_+^*+2f(\tilde{\xi})|A_+|^2A_-$$
$$+i\nabla_\perp^2A_-. \quad (6c)$$

The second-harmonic field at the cavity output is given by

$$A_2(2L)=g(\xi)A_1^2+2g(\tilde{\xi})A_+A_-. \quad (7)$$

The parameters have been rescaled as $\gamma_1t\to t$, $\sqrt{\gamma_1\tau/(2a_1L)}\mathbf{r}\to\mathbf{r}$, $E=(\eta\kappa L/\sqrt{(\gamma_1\tau)^3})\mathcal{E}_{\mathrm{in}}$, $A_1=(\kappa L/\sqrt{\gamma_1\tau})\mathcal{E}_1$, $A_2=[\kappa L/(\gamma_1\tau)]\mathcal{E}_2$, $A_\pm=(\kappa L/\sqrt{\gamma_1\tau})\mathcal{E}_\pm$, $\xi=\Delta kL$, and $\tilde{\xi}=\Delta\tilde{k}L$. The cavity loss rate of the fundamental and the parametric pairs is defined as $\gamma_1=(T+T_L)/2\tau$, where T_L accounts for any additional linear cavity losses. $\mathcal{E}_{\mathrm{in}}$ is the amplitude of the pump field external to the cavity at the fundamental frequency and can be taken to be real due to a free choice of the overall phase. The detunings $\Delta_j=(\omega_j-\omega_{j,c})/\gamma_1$, $j=1,+,-$, are defined as the difference between the frequencies of the fundamental and parametric fields, and their nearest cavity resonance frequencies normalized to the loss rate of the fundamental. Finally, the complex functions $f(\xi_1)$, $g(\xi_1)$, and $h(\xi_1,\xi_2)$ contain the dependence on the phase mismatches

$$f(\xi_1)=\frac{2i}{\xi_1}+\frac{e^{-2i\xi_1}-1}{\xi_1^2}, \quad (8a)$$

$$g(\xi_1)=\frac{e^{2i\xi_1}-1}{\xi_1}, \quad (8b)$$

$$h(\xi_1,\xi_2)=\frac{e^{2i(\xi_2-\xi_1)}-1}{\xi_2(\xi_2-\xi_1)}+\frac{e^{-2i\xi_1}-1}{\xi_1\xi_2}. \quad (8c)$$

Equations (6) were first given in [31] in a modal approximation, without the transverse Laplacians, while a mean-field equation for the OPO with a phase-mismatch-dependent nonlinear term was given in [5]. The validity of Eqs. (6) is ensured by the conditions $\gamma_1\tau\ll1$, $\Delta_j\gamma_1\tau\ll1$, $j=1,+,-$, in addition to the already mentioned assumption that diffraction and nonlinear conversion have only a small effect in a single cavity round trip.

The appearance of the cubic nonlinearity in Eq. (6a) for the fundamental and the ensuing intensity-dependent phase shift originating from the imaginary part of $f(\xi)$ is known as cascading of the fundamental field [14,20,32,33]. The induced phase shift occurs at nonzero values of the phase mismatch parameter ξ and leads to a Kerr-type nonlinearity that gives rise to bistability as discussed and observed in [20]. By investigating the sign of the imaginary part of $f(\xi)$ the non-

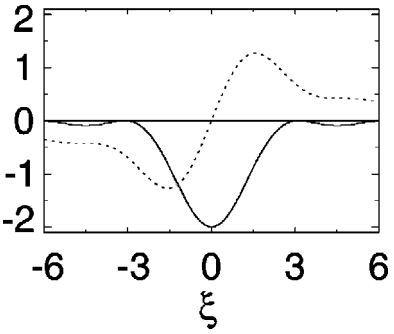

FIG. 2. The real part (full curve) and imaginary part (dotted curve) of the function $f(\xi)$.

linearity is seen to be focusing for $\xi>0$ and defocusing for $\xi<0$. The real and imaginary parts of the function $f(\xi)$ are shown in Fig. 2.

Below threshold for the competing parametric process, Eq. (6a) is of a general form that can be used to describe passive cavities with cubic nonlinearities as well as certain types of lasers [34]. For ξ an integer multiple of π, $f(\xi)$ is purely imaginary and Eq. (6a) is equivalent to the equation used in Ref. [35] to describe transverse structures in a cavity with Kerr nonlinearity.

B. Instability analysis in pure singly resonant SHG

In this section we calculate transverse-instability thresholds assuming the parametric fields are not excited. We thus put $A_+=A_-=0$ in Eqs. (6). The homogeneous solutions of the cavity equation for the fundamental field are obtained by omitting all derivatives from Eq. (6a). The resulting cubic equation is similar to the one given in [8] for doubly resonant SHG. Below the bistability threshold only one solution is physically relevant and it will be denoted A_1^0.

The homogeneous solution may destabilize above a certain pump threshold that can be obtained through a linear-stability analysis. For this purpose a general perturbation of the form $\delta A_1=\delta A e^{\lambda t+i\mathbf{k}_\perp\cdot\mathbf{r}}+\delta B e^{\lambda^* t-i\mathbf{k}_\perp\cdot\mathbf{r}}$ is introduced. After substituting into Eq. (6a) and linearizing in the perturbations a two by two matrix equation is obtained,

$$\begin{bmatrix}\lambda+M_1 & M_2\\ M_2^* & \lambda+M_1^*\end{bmatrix}\begin{pmatrix}\delta A\\ \delta B^*\end{pmatrix}=\begin{pmatrix}0\\0\end{pmatrix}, \tag{9}$$

with the definitions

$$M_1=1+i(k_\perp^2-\Delta_1)-2f(\xi)|A_1^0|^2, \tag{10a}$$

$$M_2=-f(\xi)(A_1^0)^2. \tag{10b}$$

Equation (9) has nontrivial solutions when the eigenvalue λ fulfills the following equation:

$$\lambda^2+b_1\lambda+b_2(k_\perp^2)=0, \tag{11}$$

where

$$b_1=2(1-2f_r|A_1^0|^2), \tag{12a}$$

$$b_2(k_\perp^2)=k_\perp^4-2[\Delta_1+2f_i|A_1^0|^2]k_\perp^2+(1+\Delta_1^2)+4(\Delta_1 f_i-f_r)|A_1^0|^2+3|f|^2|A_1^0|^4. \tag{12b}$$

Here subscripts r and i denote real and imaginary parts, respectively. The homogeneous solution destabilizes when the real part of the largest eigenvalue λ_r exceeds zero. Since $b_1>0$ the largest eigenvalue is given by

$$\lambda=\frac{b_1}{2}\left(-1+\sqrt{1-\frac{4b_2(k_\perp^2)}{b_1^2}}\right), \tag{13}$$

i.e., the instability threshold condition is $b_2(k_\perp^2)=0$. The imaginary part of the eigenvalue vanishes at threshold so the instability is frequency degenerate, or nonoscillatory. This is different from doubly resonant SHG where oscillatory instabilities leading to self-pulsing are found [14].

Two different types of instabilities appear in the singly resonant configuration. Assuming perturbations with $k_\perp=0$, limit points characterizing bistability of the homogeneous solutions are obtained,

$$|A_{1,b}^{0,\pm}|^2=\frac{2(f_r-\Delta_1 f_i)}{3|f|^2}\left(1\pm\sqrt{1-\frac{3|f|^2(1+\Delta_1^2)}{4(\Delta_1 f_i-f_r)^2}}\right). \tag{14}$$

Bistability is only possible when f_i and Δ_1 have opposite signs, which from Fig. 2 is seen to correspond to opposite signs of the detuning Δ_1 and the phase-mismatch parameter ξ, i.e., $\mathrm{sgn}(\xi\Delta_1)<0$. Furthermore, the absolute value of Δ_1 has to be sufficiently large. From numerical solutions the condition $|\Delta_1|\gtrsim 1.7$ is obtained.

Transverse patterns appear due to instabilities to perturbations with $k_\perp\neq 0$. An additional condition determining the transverse threshold is $\partial\lambda_r/\partial k_\perp^2=0$ or equivalently $\partial b_2/\partial k_\perp^2=0$. This gives the wave-number k_c of the perturbation with the largest growth rate. Hence, the homogeneous solutions destabilize to transverse perturbations at an intracavity amplitude given by

$$|A_{1,t}^0|^2=\frac{1}{|f|+2f_r}, \tag{15}$$

with transverse wave number

$$k_c=\sqrt{\Delta_1+2f_i|A_{1,t}^0|^2}. \tag{16}$$

Equation (15) is valid when $f_i^2>3f_r^2$. If the inequality is not satisfied there is no spatially periodic transverse instability. The amplitude of the intracavity field A_1^0 can from Eq. (6a) be related to the pump field amplitude E by

$$E^2=[1+\Delta_1^2+2(\Delta_1 f_i-f_r)|A_1^0|^2+|f|^2|A_1^0|^4]|A_1^0|^2. \tag{17}$$

The equation has been squared to avoid dependence on the phase of A_1^0.

In Fig. 3 the limit points for bistability (dotted curves) are shown together with the threshold for the transverse instability as a function of the SHG phase-mismatch parameter ξ in the case $\Delta_1=6$. Decreasing the detuning transverse instabilities, in general, exist in a smaller interval of values of pa-

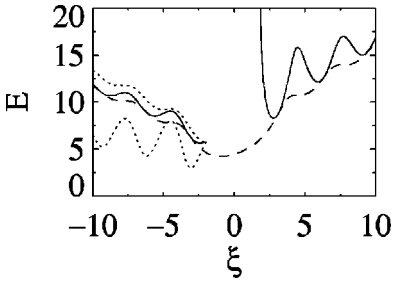

FIG. 3. The fundamental pump amplitude E necessary to reach the bistability limit points (dotted curves) and transverse-instability threshold (full curve) as a function of ξ for $\Delta_1=6$. Also shown is the threshold for the onset of the competing parametric process (dashed curve).

rameter ξ. This can be seen from Eq. (16) since a small or negative Δ_1 can lead to unphysical imaginary values of k_c. Figure 4 shows the variation of the critical wave number with ξ for three values of the fundamental detuning Δ_1.

As was already mentioned diffraction of the second-harmonic field has been neglected in the above analysis. To justify this approximation it can be included iteratively in the solution of Eq. (1b). This leads to the following second-order modification of Eq. (3) in the case where the parametric pairs are not excited:

$$\mathcal{E}_2^{(2)}(z)=\kappa\frac{e^{i\Delta kz}-1}{\Delta k}\mathcal{E}_1^2+\frac{a_2\kappa}{\Delta k}\left(\frac{e^{i\Delta kz}-1}{\Delta k}-iz\right)\nabla_\perp^2\mathcal{E}_1^2. \tag{18}$$

The extra diffractive term leads to an additional term in the mean-field equation for the intracavity amplitude. Thus Eq. (6a) for the fundamental generalizes to

$$\frac{\partial A_1}{\partial t}=(-1+i\Delta_1)A_1+f(\xi)|A_1|^2A_1+\frac{1}{2}\gamma_1\tau p(\xi)A_1^*\nabla_\perp^2A_1^2 +i\nabla_\perp^2A_1+E, \tag{19}$$

where

$$p(\xi_1)=i\frac{1+e^{-2i\xi_1}}{\xi_1^2}+\frac{e^{-2i\xi_1}-1}{\xi_1^3}. \tag{20}$$

The real and imaginary parts of $p(\xi)$ are plotted in Fig. 5. Including the extra term in the linear stability analysis leads to an equation of the same form as Eq. (9) but with modified M_i,

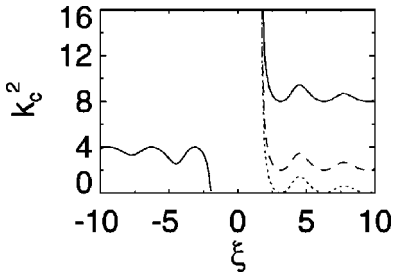

FIG. 4. The variation of the critical wave number k_c^2 with ξ for $\Delta_1=6$ (full curve), $\Delta_1=0$ (dashed curve), and $\Delta_1=-2$ (dotted curve).

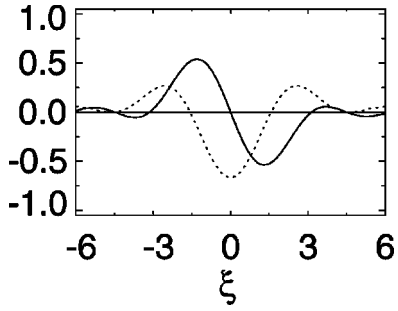

FIG. 5. The real part (full curve) and imaginary part (dotted curve) of the function $p(\xi)$.

$$M_1=1+i(k_\perp^2-\Delta_1)+|A_1^0|^2[\gamma_1\tau p(\xi)k_\perp^2-2f(\xi)], \tag{21a}$$

$$M_2=-f(\xi)(A_1^0)^2. \tag{21b}$$

The term containing the function $p(\xi)$ is seen to be negligible provided

$$\gamma_1\tau p_r(\xi)k_\perp^2|A_1^0|^2\ll 1, \tag{22a}$$

$$\gamma_1\tau p_i(\xi)|A_1^0|^2\ll 1. \tag{22b}$$

Clearly, $\gamma_1\tau\ll 1$ since this is an assumption necessary for the validity of the mean-field description. Using this together with typical threshold values of $k_\perp^2$ and $|A_1^0|^2$ from Figs. 4 and 6, and values of $p(\xi)$ from Fig. 5, the conditions are seen to hold in the threshold analysis for almost all values of the SHG phase-mismatch parameter ξ. Only in the very limited region close to the boundary of existence of the transverse instability might the approximation not be appropriate. However, this region is not of great interest due to the corresponding dramatic increase in the instability threshold and leads, in addition, to a breakdown of the assumptions made for the mean-field description. Similar argumentation can be used to neglect the iterative terms in the analysis of the mean-field equations for $A_\pm$ presented in the next section. This demonstrates the consistency of Eqs. (6) for the presented threshold calculations.

C. Competing parametric process

The threshold for the competing parametric oscillation is calculated in this section. It can be obtained from a stability analysis of the ground-state solutions $A_\pm=0$, by intro-

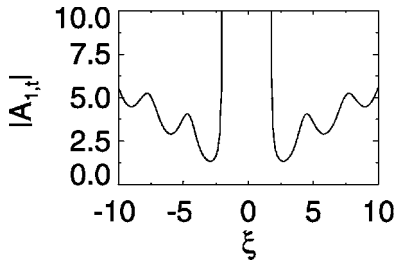

FIG. 6. The variation of the intracavity fundamental intensity with ξ. From Eq. (15) $|A_{1,t}^0|^2$ is found to be independent of the fundamental detuning Δ_1. However, only values of ξ and Δ_1 where k_c is real and positive correspond to an instability.

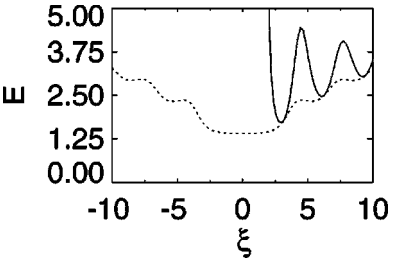

FIG. 7. The transverse instability threshold (full curve) and the threshold for the parametric process (dotted curve) as a function of ξ for $\Delta_1=0$.

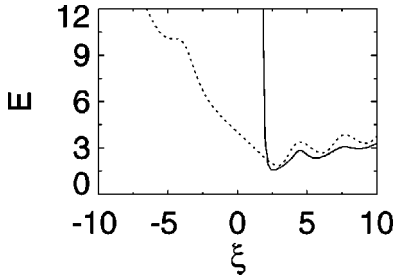

FIG. 8. The transverse instability threshold (full curve) and the threshold for the parametric process (dotted curve) for $\Delta_1=-2$. The bistability is not shown since it appears almost on top of the transverse instability.

ducing the perturbations $A_+=\delta A_+ e^{\tilde{\lambda}t+i\tilde{\mathbf{k}}_\perp\cdot\mathbf{r}}$ and $A_-=\delta A_- e^{\tilde{\lambda}^* t-i\tilde{\mathbf{k}}_\perp\cdot\mathbf{r}}$. The calculation is similar to the one presented in [36] and leads to the threshold

$$|A_{1,p}^0|^2=\frac{\sqrt{1+(\tilde{k}_\perp^2-\Delta_1)^2}}{|h(\tilde{\xi},\xi)|}. \tag{23}$$

Here, energy conservation expressed as $\Delta_+ + \Delta_- = 2\Delta_1$ has been used.

The parameter $\tilde{\xi}$ is free in the sense that the parametric pair with the largest gain (lowest threshold) will be selected. Therefore, the threshold for onset of parametric oscillation is obtained from Eq. (23) by maximizing $|h(\tilde{\xi},\xi)|$ with respect to $\tilde{\xi}$, which leads to $\tilde{\xi}=0$ or $\tilde{\xi}=\xi$. Since the down-converted frequencies are assumed to be within the phase-matching bandwidth of the fundamental frequency $\xi=\tilde{\xi}$ can be fulfilled. We find $|h(\tilde{\xi}=0,\xi)|=|h(\tilde{\xi}=\xi,\xi)|=|e^{2i\xi}-2i\xi-1|/\xi^2$. Similarly, the parametric photons will be emitted with the value of the transverse wave-number $\tilde{k}_\perp$, which lowers the threshold. For positive detuning $\Delta_1>0$ the critical wave-number $\tilde{k}_\perp=\sqrt{\Delta_1}$ is selected leading to off-axis emission. In the case of negative detuning $\tilde{k}_\perp=0$, and the down-converted fields have a homogeneous spatial structure.

In Fig. 7 the threshold for the parametric process is plotted at resonance ($\Delta_1=0$) together with the threshold for the transverse instability. Here, the parametric-generation threshold is seen to be below the pattern-forming threshold. This was also found to be the case for almost all values of ξ for $\Delta_1=6$ (Fig. 3). Thus, the limitation of the pure SHG calculation presented in the previous section is pointed out, and a more general analysis would also have to include nonvanishing amplitudes of the parametric fields. However, it is worth noticing that the pure SHG description is a good approximation when describing the behavior close to the parametric threshold where the parametric term in Eq. (6a) is negligible compared to the cubic nonlinearity of the fundamental field. Furthermore, it is possible to choose the fundamental detuning so that the transverse instability threshold is below the parametric threshold for all values of ξ and thus the pure SHG description is strictly valid. An example is given in Fig. 8 for $\Delta_1=-2$.

It is worth emphasizing that apart from complicating the analysis of the linear instability thresholds, the existence of the competing parametric process can have a strong nonlinear influence on the subsequent pattern formation. Indeed, the mentioned off-axis emission of parametric pairs is a mechanism for pattern formation in the ordinary OPO. This is also the case in the subharmonic pumped OPO as is demonstrated numerically in the next section.

III. NUMERICAL ANALYSIS

A. Singly resonant SHG

In this section we study the above-threshold behavior numerically, assuming that the parametric process does not participate in the dynamics. We thus solve the equation

$$\frac{\partial A_1}{\partial t}=(-1+i\Delta_1)A_1+f(\xi)|A_1|^2A_1+i\nabla_\perp^2 A_1+E. \tag{24}$$

In this approximation the second-harmonic field is given by $A_2(2L)=g(\xi)A_1^2$.

As already noted this equation is of the same type as those that arise in descriptions of driven cavities containing a medium with cubic nonlinearity [34,35]. We thus expect, and indeed find, spatial structures including periodic patterns and localized states, which are known from previous studies of nonlinear cavities. Equation (24) was solved using a split-step algorithm on a square domain with periodic boundary conditions and a constant, position-independent pump amplitude E. Grid sizes of 32×32 up to 128×128 points were used. The forcing, linear, and nonlinear terms were solved in real space using a Runge-Kutta routine, while the diffractive term was solved in Fourier space. As a check on the results an alternative operator splitting where the forcing and linear terms were accounted for in Fourier space was also used. No significant numerical difference was found between the two approaches. The dynamics were seeded by starting the calculation with a small amount of random noise in the cavity field A_1, and then integrating until the temporal transients had died out. Integration was stopped when the calculated mean and peak amplitudes were stable to an accuracy of at least 10^{-4}. Depending on parameters typical time steps were 10^{-3}–10^{-4} and integration times to reach stationary conditions were up to several thousand time units.

Figure 9 shows an example of hexagonal pattern formation for a focusing nonlinearity with $\Delta_1=-2$ and $\xi=4.5$. For these parameters the mean intracavity amplitude is a single-valued function of the pump amplitude E. From Fig. 9 we see that this corresponds to a situation where the parametric threshold is higher than that of the transverse instabil-

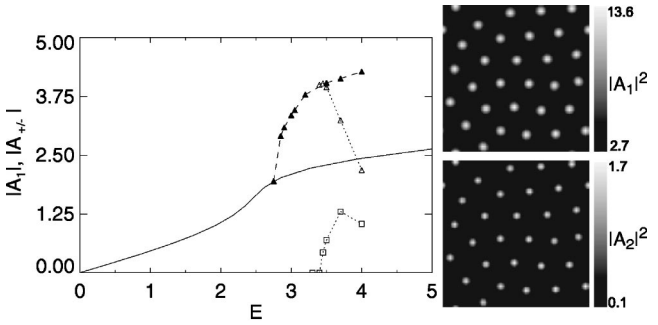

FIG. 9. Hexagonal patterns in a pure SHG for $\Delta_1=-2$ and $\xi=4.5$. The solid line is the plane-wave solution of Eq. (17) while the filled triangles give the maximum value of $|A_1|$. The open triangles are the maximum value of $|A_1|$ in the presence of parametric down conversion, while the open squares give the maximum value of $|A_\pm|$. The calculations were made on a square domain of size 25×25.

ity, so that Eq. (24) is a good approximation. From Eqs. (15) and (17) the threshold for transverse instability occurs at $E\simeq2.85$, which agrees closely with the onset of instability observed numerically. The hexagonal patterns seen in both the fundamental and second-harmonic fields were obtained after integrating for several hundred time constants. These patterns are sometimes free of defects, and sometimes contain a few, depending on the initial conditions and integration time. The patterns appear as a modulation on a uniform background for both the fundamental and the second-harmonic field. Since the second harmonic leaving the cavity is proportional to the intracavity field squared, the pattern appears on top of a relatively weaker background, than does the pattern in the fundamental.

For other values of detuning and phase mismatch either transverse instabilities or parametric generation may have the lowest threshold. However, when Δ_1 is non-negative and $\xi=n\pi$ with n integer, the two thresholds are strictly equal and the pure SHG approximation is a reasonable one close to threshold. An example of pattern formation in such a case for $\Delta_1=6$ and $\xi=6.1$ (for which the intracavity amplitude is single valued) is shown in Fig. 10. There are branches with apparently stable hexagonal and square patterns that can be accessed by changing the initial conditions or the pump amplitude.

An additional numerical check on the validity of the mean-field model was made in the pure SHG limit by directly integrating propagation Eqs. (1a) and (1b) from $z=0$ to $z=2L$, updating the fields in time at $z=2L$ with boundary

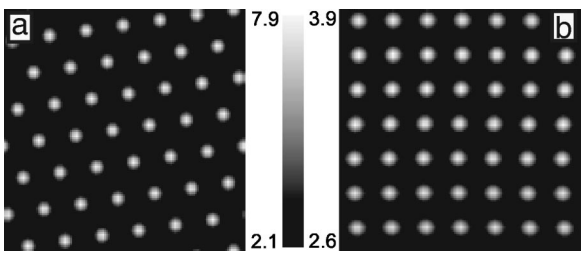

FIG. 10. Intensity distribution of the second-harmonic field $|A_2(2L)|^2$ for $\Delta_1=6$ and $\xi=6.1$. (a) $E=13.20$ and (b) $E=12.25$. The window size is 15×15.

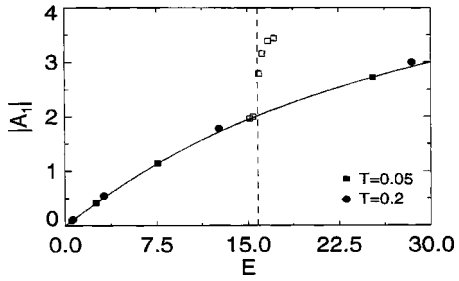

FIG. 11. Comparison of mean-field and propagation equation calculations for $\Delta_1=6$ and $\xi=4.5$. The solid line shows the mean-field result for the plane-wave intracavity amplitude from Eq. (17) while the filled squares and circles are numerical results obtained from Eqs. (25) and (26). The open squares show the peak amplitude of the hexagonal pattern in the fundamental field and the vertical dotted line indicates the mean-field result for the threshold of transverse instability. Mean-field and propagation equation results were plotted on the same figure using the relations $A_1=\sqrt{2/T}A_{1P}$ and $E=(\sqrt{8}/T^{3/2})E_P$.

conditions corresponding to the input coupler, propagating the fields again, and so on. Although this direct approach is generally more time consuming than solving the mean-field equations since we calculate the fields as functions of (x,y,z,t) instead of just (x,y,t) in the mean-field model, it has the advantage of being correct, even when the approximations leading to the mean-field model break down. Rescaling the variables in Eqs. (1a) and (1b) as $A_{1P}=\kappa L\mathcal{E}_1$, $A_{2P}=i\kappa L e^{-i\Delta kz}\mathcal{E}_2$, $z_P=z/L$, and $\mathbf{r}_P=(2k_1/L)^{1/2}\mathbf{r}$, and neglecting the parametric fields, gives the normalized set

$$\frac{\partial A_{1P}^{(m)}}{\partial z_P}-i\nabla_{\perp P}^2A_{1P}^{(m)}=A_{1P}^{(m)*}A_{2P}^{(m)}, \tag{25a}$$

$$\frac{\partial A_{2P}^{(m)}}{\partial z_P}-\frac{i}{2}\nabla_{\perp P}^2A_{2P}^{(m)}+i\xi A_{2P}^{(m)}=-A_{1P}^{(m)2}. \tag{25b}$$

In Eq. (25) the fields are functions of the continuous spatial variables (x,y,z) and the discrete time variable $t_m=m\tau$ indicated by the superscript.

These are solved together with the normalized cavity boundary conditions

$$A_{1P}^{(m+1)}(\mathbf{r}_P,z_P=0)=E_P+\sqrt{1-T}e^{i\Delta_{1P}}A_{1P}^{(m)}(\mathbf{r}_P,z_P=2), \tag{26a}$$

$$A_{2P}^{(m)}(\mathbf{r}_P,z_P=0)=0, \tag{26b}$$

where $E_P=\sqrt{T}\kappa L\mathcal{E}_{\rm in}$ and $\Delta_{1P}=(T/2)\Delta_1$.

Figure 11 compares the mean-field and propagation calculation results for the homogeneous intracavity amplitude (neglecting diffraction) as a function of pump amplitude E. For the parameters used the mean-field result for the threshold for transverse instability of the fundamental is $E_t=15.8$ (see Fig. 14 below). Calculations are given for cavity transmission losses of $T=0.05$ and 0.2. For the smaller transmission value there is no visible difference betweeen mean-field and Maxwell equation results. Even for $T=0.2$, which is many times higher than typical experimental values of the cavity transmission (see Sec. IV B), there is only a few per-

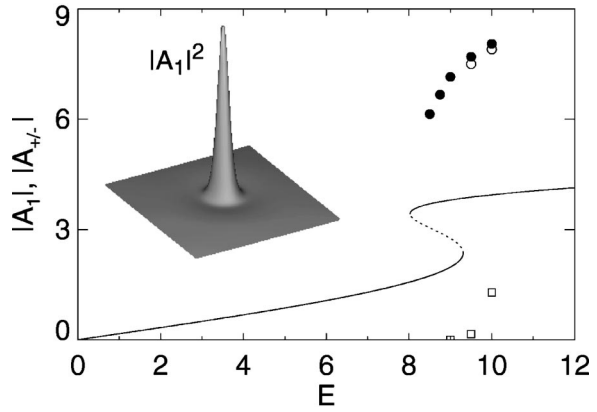

FIG. 12. Localized states obtained for $\Delta_1=-6$ and $\xi=4.5$. The solid (dashed) line is the stable (unstable) part of the plane-wave solution of Eq. (17). The filled circles give the maximum value of $|A_1|$, the open circles are the maximum value of $|A_1|$ when the parametric process is allowed, and the open squares are the maximum value of $|A_\pm|$. The inset shows $|A_1|^2$ on a window of size 9×9.

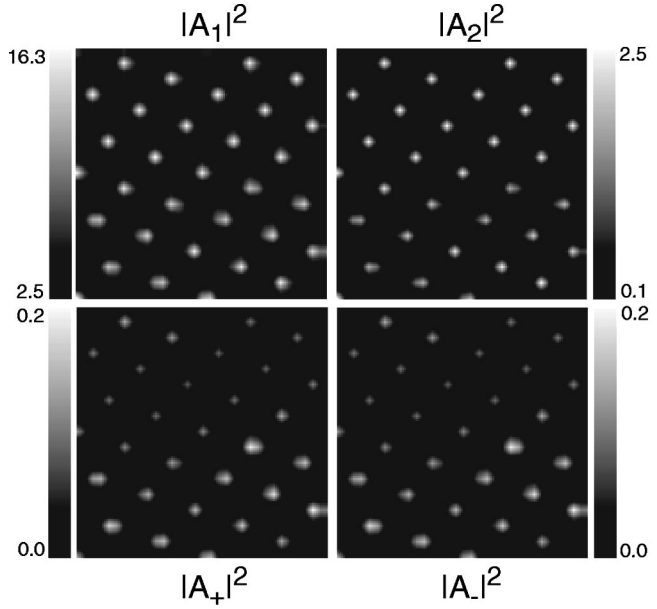

FIG. 13. Intensity distribution of all four fields obtained for the parameters of Fig. 9, and $E=3.45$.

cent difference between the two calculations at a pump amplitude about twice the transverse instability threshold.

Numerical results for instability thresholds, spatial structures, and characteristic transverse wave number, were generally consistent with the results obtained from the mean-field equations. For example the mean-field prediction for the wave number of the transverse instability for the parameters of Fig. 11 is $k_c=3.07$. Numerical solution of the propagation equations with $T=0.05$ resulted in a periodic hexagonal pattern with (after rescaling to mean-field values) $k_{cP}\simeq 3.3$, which agrees to within 10% of the mean-field analysis. The peak amplitude of the hexagonal pattern as a function of the pump amplitude is shown by the open squares in Fig. 11 (compare with the filled squares in Fig. 14 for the mean-field result). The pump amplitude at the threshold of transverse instability as calculated from the mean-field theory and propagation equations is also seen to agree closely. A more detailed comparison of results obtained from propagation equations with the predictions of the mean-field description will be given elsewhere.

Localized states, also called cavity solitons, appear for parameter values where the plane-wave solution exhibits bistability. Looking for conditions where the parametric threshold is equal to that of the transverse instability would suggest choosing $\xi=n\pi$. However, $f(\xi)$ is then purely imaginary and we recover the Kerr limit of Eq. (24) in which case cavity solitons are unstable [37]. We choose, therefore, a somewhat different value of ξ that adds an effective absorptive component to the nonlinearity, and leads to stable cavity solitons [38].

Figure 12 gives an example of a localized state obtained for $\Delta_1=-6$ and $\xi=4.5$. For these parameter values the system is bistable. The solution was seeded by adding a Gaussian perturbation to the driving field E with a width similar to the localized state. The Gaussian seed was switched off after a few time constants, after which the evolution was followed numerically. The depicted solution has only very weak rings around the central lobe and was stable for hundreds of time constants. For more vigorous initial seeding solutions with several coexisting localized states were obtained.

B. Singly resonant SHG with parametric generation

In this section we investigate the validity of the pure SHG description of the cavity dynamics. We thus solve Eqs. (6) for the intracavity fields, and use Eq. (7) for the resulting second harmonic. In the calculations below we have for simplicity taken $\Delta_+=\Delta_-=\Delta_1$, and, in order to minimize the parametric threshold, $\tilde{\xi}=\xi$.

One effect of the competing parametric generation is to damp the patterns at high values of the pump parameter. This is seen in Fig. 9 where the open triangles and squares show the maximum amplitudes of the fundamental and parametric fields as a function of the pump amplitude E. The threshold for parametric generation is $E\simeq 3.40$. Below this point the parametric fields are unexcited. As the pump amplitude is increased beyond this threshold the parametric fields grow

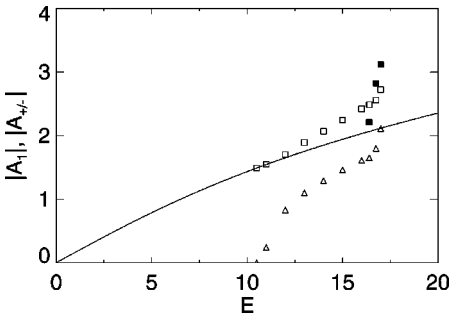

FIG. 14. Dependence of the intracavity fields on the pump amplitude when the parametric threshold is lower than that of the SHG transverse instability. $\Delta_1=6$ and $\xi=4.5$. The solid line is the plane-wave solution of Eq. (17), the filled squares give the maximum value of $|A_1|$ without parametric oscillation, the open squares give the maximum value of $|A_1|$ with parametric oscillation, and the open triangles give the maximum value of $|A_\pm|$.

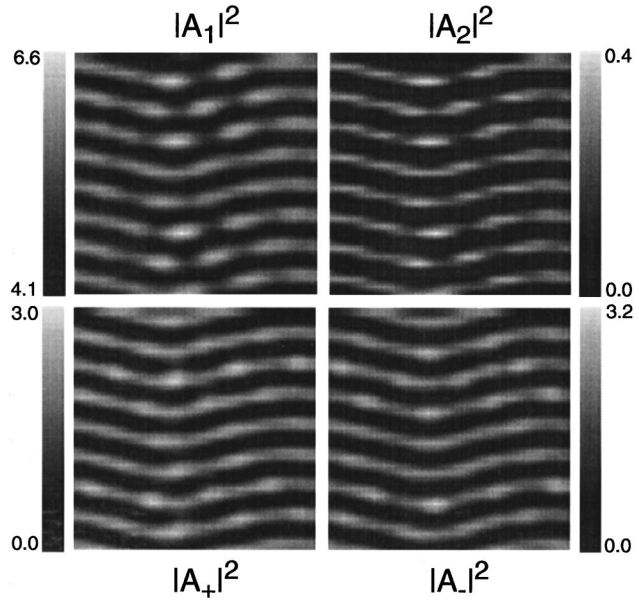

FIG. 15. Intensity distributions for the same parameters as Fig. 14 at $E=16.75$. The intracavity amplitude is a single-valued function of the pump amplitude. The window size is 12×12.

while the intracavity fundamental decreases. Thus, the main effect of the parametric process in this situation is to decrease the level of the intracavity field. The parametric fields are modulated with the same hexagonal symmetry seen in the fundamental and second-harmonic fields as shown in Fig. 13 obtained for $E\simeq3.45$. The figure was obtained before complete relaxation of the fields so that some nonuniformity, particularly in the parametric fields, is visible. The two parametric fields are seen to have very similar intensity distributions. Note also that they appear on a vanishing background, as opposed to the fundamental and second harmonics. For pump amplitudes of $E\sim4$ and higher the maximum amplitudes of both the fundamental and the parametric fields saturate and even fall slightly. At these high-pump conditions the hexagonal symmetry is no longer perfect, and defects in the patterns appear.

The parametric process can also be excited below the threshold of transverse instability. In Fig. 14 we have taken $\Delta_1=6$ and $\xi=4.5$ that gives a parametric generation threshold at $E_p=10.7$, while the fundamental first becomes transversely unstable at $E_t=15.8$. The numerical results reveal that the fundamental and parametric beams take on finite values for $E>E_p$; however, there is no spatial structure. The fundamental is emitted as an on-axis plane wave while the parametric beams are emitted as plane waves with an angular tilt given by $k_c=\pm\sqrt{\Delta_1}$. Thus, below E_t the subharmonic-pumped OPO exhibits the same features as the second-harmonic-pumped OPO [5]. When $E>E_t$ transverse instability sets in, and there is a cooperative effect leading to a sharp rise in the peak amplitude of the parametric fields, as seen in Fig. 14. For E not too far above E_t roll structures, with some transverse modulation are seen, as shown in Fig. 15. Increasing E further leads to patterns with predominantly square symmetry.

Finally, we show in Fig. 16 that localized states can coexist in the four interacting fields. The parameters were the same as those used in Fig. 12, except that strong initial seeding was used to generate multiple solitons. The parametric threshold for the parameters of the figure is at $E\simeq8.7$, which coincides within a few percent with the onset of parametric cavity solitons seen numerically. Generation of solitons in the parametric fields serves also to dampen slightly the peak amplitude of the fundamental solitons, as seen in Fig. 12, where the data points were obtained for the case of a single soliton in the computation window.

IV. EXPERIMENTAL FEASIBILITY

In this section we discuss the experimental feasibility of observing transverse instabilities in singly resonant SHG. In Sec. IV A the effect of propagation losses of a Gaussian pump beam in a plane cavity is accounted for, while numerical estimates of the pattern formation threshold are given in Sec. IV B.

A. Propagation losses

In the theoretical model the electric-field amplitudes were treated as plane waves. In a real experiment the propagation spread of a Gaussian beam inside the plane cavity will lead to effectively lower buildup compared to the plane-wave expression. This can be a serious problem if the Rayleigh length of the Gaussian beam is not sufficiently large compared to the cavity length, since the fields effectively experience many roundtrips in the cavity. The importance of the propagation losses will in the following be investigated by numerical integration of the Gaussian beam propagation equations.

We define the intracavity build-up factor as the ratio of the intracavity power to the external pump power: $B=P_c/P_p$. The plane-wave expression is given by

$$B_{PW}=\frac{T}{\left(1-\sqrt{1-T-T_L}+\frac{1}{2}P_cE_{NL}\right)^2}, \tag{27}$$

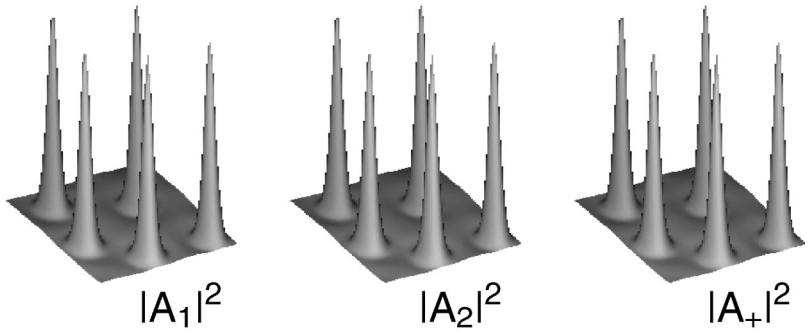

FIG. 16. Localized states coexisting in all four fields. The spatial distribution of $|A_-|^2$ was the same as that in the other fields. The plots have been scaled to give the same visual height in each field. The parameters were the same as in Fig. 12 and the pump amplitude was $E=10$.

with the nonlinearity of the crystal defined through the coefficient $E_{NL}=P_2/P_1^2$, where P_2 is the power generated from an input P_1 in a single-pass propagation through the cavity of length $2L$. Thus, $P_c E_{NL}$ is the nonlinear loss of the fundamental, which adds to the transmission loss. For the experimental parameters presented below the nonlinear loss turns out to be completely negligible compared to passive losses and can, therefore, be omitted in the following. The intracavity electric field of the Gaussian beam is calculated from

$$E_{\mathrm{tot}}=\sqrt{T}\sum_{m=0}^{\infty}(1-T)^{m/2}(1-T_L)^{m/2}E(r,z=2mL). \quad (28)$$

Here, the Gaussian beam field amplitude is given by

$$E(r,z)=\frac{A}{1+z/q_0}e^{i(n\pi/\lambda_0)[1/(q_0+z)]r^2}, \quad (29)$$

with amplitude A and complex parameter $q_0=-in\pi w_0^2/\lambda_0$ assuming the beam waist is positioned at $z=0$. The build-up factor for a Gaussian beam B_{GB} is obtained by integrating the modulus of the total electric field $|E_{\mathrm{tot}}|^2$ over the transverse plane to get the power and dividing by the input pump power

$$B_{GB}=\frac{\int_0^\infty r|E_{\mathrm{tot}}(r)|^2dr}{\int_0^\infty r|A|^2e^{-2r^2/w_0^2}dr}. \quad (30)$$

Sum (28) is calculated numerically. The necessary number of terms to include depends on the value of the input coupler transmission T; typically, about 5000 terms were sufficient. Numerical estimates of the importance of the propagation loss are given in the following section.

B. Physical parameters corresponding to an instability threshold

In order to relate the calculated thresholds to experimental parameters we will consider the case of noncritically temperature phase-matched SHG in potassium niobate where the effective nonlinearity coefficient is $d_{\mathrm{eff}}=21$ pm/V [39]. The coefficient κ introduced in Eqs. (1) is given by $\kappa=\omega_1 d_{\mathrm{eff}}/nc$, where ω_1 is the frequency of the fundamental field taken to be 2.2×10^{15} Hz corresponding to a wavelength $\lambda_0=860$ nm, and $n\simeq2.3$ is the refractive index. Furthermore, a cavity length $L=1$ cm is assumed in addition to a typical residual round-trip loss of $T_L=1\%$. The waist radius w_0 of the fundamental beam is determined by a tradeoff since focusing is needed to enhance the nonlinearity while too narrow focusing is not allowed in order to observe spatial structures. The spatial period of the transverse structure is $\Lambda=2\pi/k_c$ and the number of spatial periods within the Gaussian envelope of the pump beam is defined as $l=2w_0/\Lambda$. Notice, k_c now denotes the critical wave number in the original unscaled parameters and the relation to the scaled quantity $\overline{k_c}$ is $k_c=\overline{k_c}\sqrt{\gamma_1\tau k_1/L}$. This leads to $w_0=(\pi l/\overline{k_c})\sqrt{2L/[(T+T_L)k_1]}$.

Taking also the propagation loss into account as described in the previous section the expression for the fundamental pump power necessary to reach the instability threshold is given by

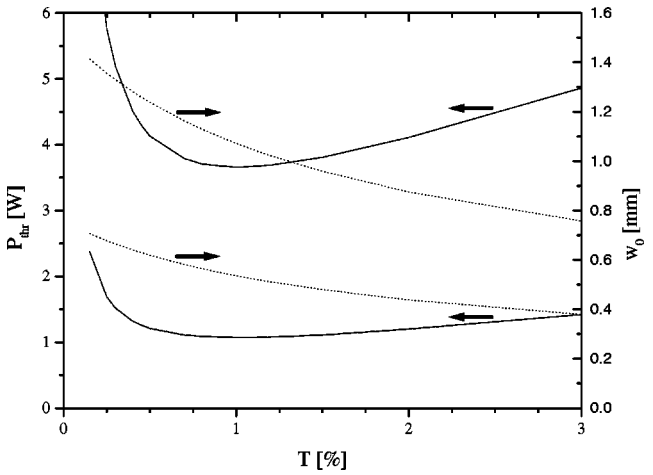

FIG. 17. The pump power necessary to reach the transverse-instability threshold (full curves) and the corresponding waist (dotted curve) as a function of the transmission of the input coupler T for $l=1$ (lower curves) and $l=2$ (upper curves).

$$P_1=\frac{\epsilon_0 nc}{2}\frac{\pi w_0^2}{2}\frac{B_{PW}}{B_{GB}}|\mathcal{E}_{in}|^2$$
$$=\frac{\epsilon_0 n^2c^4\pi^3l^2}{16\overline{k_c}^2\omega_1^3d_{\mathrm{eff}}^2L}\frac{(T+T_L)^2}{T}\frac{B_{PW}}{B_{GB}}E^2, \quad (31)$$

where ϵ_0 is the vacuum permittivity. From Fig. 7 the lowest threshold is found to be at $\xi=2.9$ where $E=1.7$ or $|A_{1,t}^0|=1.2$ corresponding to $\overline{k_c}=1.4$ (Fig. 4). Figure 17 shows the threshold power needed to reach instability and the corresponding waist as a function of the transmission of the input coupler T for $l=1,2$. The optimum input coupler choice $T=T_L$ corresponds to impedance matching of the cavity. The lowest threshold appears to be on the order of 1 W, which should be readily attainable with existing high power near infrared continuous wave lasers. The corresponding generated blue power is about 1 mW. The very poor conversion efficiency of the process is due to the introduced phase mismatch and weak focusing necessary for observing transverse structures. The effect of including the propagation losses led to a threshold power increase of about 15% for $l=1$ and 2% for $l=2$ compared to the plane-wave calculation.

In the above analysis the phase-matching bandwidth of the crystal was not taken into account. Indeed we assumed $\xi=\tilde{\xi}$ could be fulfilled. In a short cavity the parametric pairs positioned an integer multiple of the free-spectral cavity length away from the fundamental frequency may lie outside the phase-matching bandwidth. From [39] the phase-matching bandwidth for a 2-cm-long potassium niobate crystal phase matched at 860 nm can be found to be $\delta\omega_{bw}=64$ GHz. This should be compared with the free-spectral range $\omega_{FSR}=41$ GHz of the cavity. Thus, an increased threshold for the parametric pairs is expected. Both the phase-matching bandwidth and the free-spectral range scale as $1/L$, i.e., the analysis holds for all monolithic cavities. A

nonmonolithic cavity could be used to avoid increasing the parametric threshold.

V. CONCLUSIONS

In this paper pattern formation in phase-mismatched SHG in a plane-plane cavity, resonant only for the fundamental field, has been investigated. Instability thresholds for bistability and transverse pattern formation were calculated. The possibility of the second-harmonic field serving as a pump for a competing parametric down-conversion process was investigated. Parameter regimes were identified where either transverse instability of pure SHG or parametric generation have the lowest threshold. In the former case numerical analysis revealed periodic patterns, as well as localized structures, similar to those found earlier in doubly resonant intracavity SHG. The presence of parametric generation affects the amplitude of the generated patterns, but does not change their spatial structure.

Alternatively, when the parametric threshold is lower than that of the transverse instability the parametric process also influences the spatial structure of the patterns. Below the transverse-instability threshold the normal picture of parametric generation of tilted plane waves is observed. When the pump amplitude is increased beyond the transverse-instability threshold the parametric process affects the spatial patterns so that roll-like structures are seen, instead of the hexagons or squares otherwise observed in SHG. In addition to periodic patterns, excitation of cavity solitons is possible. Depending on the parameters chosen they can exist in pure SHG, or in all four fields simultaneously. Finally, numerical estimates of the pump power necessary to reach transverse instability given realizable experimental parameters were given. The thresholds are considerably higher than in a doubly resonant SHG, yet attainable with available continuous-wave laser sources.

ACKNOWLEDGMENTS

Support for this work was provided by the Danish Natural Science Research Council. P.L. acknowledges support from the Danish Research Academy and thanks S. Schiller for helpful discussions.

[1] For a review of optical pattern formation see, for example, L. A. Lugiato, Chaos Solitons Fractals **4**, 1251 (1994).
[2] S. E. Harris, Appl. Phys. Lett. **9**, 114 (1966).
[3] G.-L. Oppo, M. Brambilla, and L. A. Lugiato, Phys. Rev. A **49**, 2028 (1994).
[4] K. Staliunas, J. Mod. Opt. **42**, 1261 (1995).
[5] S. Longhi, J. Mod. Opt. **43**, 1089 (1996).
[6] S. Longhi, Phys. Rev. A **53**, 4488 (1996).
[7] S. Longhi, J. Mod. Opt. **43**, 1569 (1996).
[8] C. Etrich, U. Peschel, and F. Lederer, Phys. Rev. E **56**, 4803 (1997).
[9] P. M. Lushnikov, P. Lodahl, and M. Saffman, Opt. Lett. **23**, 1650 (1998).
[10] G. J. de Valcárcel, K. Staliunas, E. Roldán, and V. J. Sánchez-Morcillo, Phys. Rev. A **54**, 1609 (1996).
[11] S. Longhi, Phys. Scr. **56**, 611 (1997).
[12] K. Staliunas and V. J. Sánchez-Morcillo, Phys. Rev. A **57**, 1454 (1998).
[13] C. Etrich, U. Peschel, and F. Lederer, Phys. Rev. Lett. **79**, 2454 (1997).
[14] P. D. Drummond, K. J. McNeil, and D. F. Walls, Opt. Acta **27**, 321 (1980).
[15] S. Longhi, Opt. Lett. **23**, 346 (1998).
[16] U. Peschel, D. Michaelis, C. Etrich, and F. Lederer, Phys. Rev. E **58**, R2745 (1998); C. Etrich, D. Michaelis, U. Peschel, and F. Lederer, *ibid.* **58**, 4005 (1998).
[17] E. S. Polzik, J. Carri, and H. J. Kimble, Phys. Rev. Lett. **68**, 3020 (1992).
[18] S. F. Pereira, M. Xiao, H. J. Kimble, and J. L. Hall, Phys. Rev. A **38**, 4931 (1988).
[19] L. A. Lugiato and A. Gatti, Phys. Rev. Lett. **70**, 3868 (1993); A. Gatti and L. A. Lugiato, Phys. Rev. A **52**, 1675 (1995); A. Gatti, H. Wiedemann, L. Lugiato, I. Marzoli, G.-L. Oppo, and S. M. Barnett, *ibid.* **56**, 877 (1997).
[20] A. G. White, J. Mlynek, and S. Schiller, Europhys. Lett. **35**, 425 (1996).
[21] R. Paschotta, M. Collett, P. Kürz, K. Fiedler, H. A. Bachor, and J. Mlynek, Phys. Rev. Lett. **72**, 3807 (1994).
[22] H. Tsuchida, Opt. Lett. **20**, 2240 (1995).
[23] S. Longhi, Opt. Commun. **153**, 90 (1998).
[24] M. A. M. Marte, Phys. Rev. A **49**, R3166 (1994).
[25] A. Eschmann and M. A. M. Marte, Quantum Semiclassic. Opt. **9**, 247 (1997).
[26] S. Schiller and R. L. Byer, J. Opt. Soc. Am. B **10**, 1696 (1993).
[27] S. Schiller, G. Breitenbach, R. Paschotta, and J. Mlynek, Appl. Phys. Lett. **68**, 3374 (1996).
[28] M. A. M. Marte, Phys. Rev. Lett. **74**, 4815 (1995); J. Opt. Soc. Am. B **12**, 2296 (1995).
[29] J. L. Sørensen and E. S. Polzik, Appl. Phys. B: Lasers Opt. **66**, 711 (1998).
[30] L. A. Lugiato, Prog. Opt. **21**, 71 (1984).
[31] S. Schiller, R. Bruckmeier, and A. G. White, Opt. Commun. **138**, 158 (1997).
[32] R. DeSalvo, D. J. Hagan, M. Sheik-Bahae, G. Stegeman, E. W. Van Stryland, and H. Vanherzeele, Opt. Lett. **17**, 28 (1992).
[33] K. Kasai, G. Jiangrui, and C. Fabre, Europhys. Lett. **40**, 25 (1997).
[34] L. A. Lugiato and C. Oldano, Phys. Rev. A **37**, 3896 (1988); M. Tlidi, M. Georgiou, and P. Mandel, *ibid.* **48**, 4605 (1993).
[35] A. J. Scroggie, W. J. Firth, G. S. McDonald, M. Tlidi, R. Lefever, and L. A. Lugiato, Chaos Solitons Fractals **4**, 1323 (1994).
[36] G.-L. Oppo, M. Brambilla, D. Camesasca, A. Gatti, and L. A. Lugiato, J. Mod. Opt. **41**, 1151 (1994).
[37] W. J. Firth and A. Lord, J. Mod. Opt. **43**, 1071 (1996).
[38] W. J. Firth and A. J. Scroggie, Phys. Rev. Lett. **76**, 1623 (1996).
[39] J. C. Baumert, P. Günter, and H. Melchior, Opt. Commun. **48**, 215 (1983).